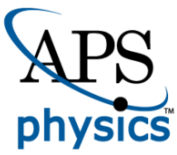

Giant Anomalous Hall Effect due to Double-Degenerate Quasiflat Bands

Wei Jiang, Duarte J. P. de Sousa, Jian-Ping Wang, and Tony Low

Phys. Rev. Lett. **126**, 106601 — Published 10 March 2021

DOI: 10.1103/PhysRevLett.126.106601

Giant Anomalous Hall Effect due to Double-Degenerate Quasi Flat Bands

Wei Jiang,[1,*] Duarte J. P. de Sousa,[1] Jian-Ping Wang,[1] and Tony Low[1,†]

[1] *Department of Electrical & Computer Engineering, University of Minnesota, Minneapolis, Minnesota 55455, USA.*

(Dated: December 7, 2020)

Abstract

We propose a novel approach to achieve giant AHE in materials with flat bands (FBs). FBs are accompanied by small electronic bandwidths, which consequently increases the momentum separation ($\mathcal{K}$) within pair of Weyl points and thus the integrated Berry curvature. Starting from a simple model with a single pair of Weyl nodes, we demonstrated the increase of $\mathcal{K}$ and AHE by decreasing bandwidth. It is further expanded to a realistic pyrochlore lattice model with characteristic double degenerated FBs, where we discovered a giant AHE while maximizing the $\mathcal{K}$ with nearly vanishing band dispersion of FBs. We identify that such model system can be realized and modulated through strain engineering in both pyrochlore and spinel compounds based on first-principles calculations, validating our theoretical model and providing a feasible platform for experimental exploration.

Introduction The anomalous Hall effect (AHE), i.e., a zero field Hall conductivity observed in ferromagnetic materials mediated by spin-orbit coupling (SOC), is one of the most intriguing electronic transport phenomena [1]. It has been proposed for magnetic sensors and memories for their high sensitivity and thermal stability [2–4] and energy efficient spintronics applications [5–8]. There are two prevalent explanations, i.e., intrinsic AHE due to SOC and extrinsic AHE due to impurity scattering [1, 9–13]. The theory of intrinsic AHE was first put forth by Karplus and Luttinger [14], and subsequently better appreciated due to Berry curvature of the occupied Bloch bands [11, 12, 15, 16]. More recently, with the discovery of various topological states, Weyl semimetal (WSM) systems have been touted as fertile ground for large AHE as Weyl points and their vicinity can host large Berry curvature [17–20]. Large AHE has indeed been observed in several material candidates that have been studied both theoretically and experimentally [21–23]. Several rule of thumb have been suggested for achieving high AHE, however, there is no consensus on their general applicability [22–24].

Theory has elaborated that the intrinsic peak anomalous Hall conductivity (AHC) in WSMs with single pair of Weyl nodes is given by $\sigma_{xy} = \frac{e^2\mathcal{K}}{4\pi^2}$, where $\mathcal{K}$ is the momentum separation between Weyl nodes [18]. To maximize AHE, an apparent approach would be to increase $\mathcal{K}$, which could be tuned through band engineering. In general material systems, there are usually multiple pairs of Weyl nodes, which are located at different energy due to the dispersing bands. Consequently, their corresponding AHC as a function of energies usually shows multiple peaks and the Fermi level is rarely coincident with the AHC peak. In this work, we show that the simultaneous harvesting of maximal Berry curvatures from multiple pairs of Weyl points can be achieved through engineering of flat bands (FBs) [25–27]. These FBs present limited electronic bandwidth where the Fermi level and peak AHC coincides, and at the same time maximizes the Weyl points separation $\mathcal{K}$.

FB systems would be ideal considering their intrinsic dispersionless bands. The pinning of the Fermi level to the FB would also be easier to achieve due to its large density of states. Strongly-correlated FB in low dimensions (1D or 2D) has been extensively studied, yielding various exotic quantum states, e.g., ferromagnetism, superconductivity, and topological states [25–32]. Recent studies have looked into 3D FB and various topological states [33–38]. However, there are no study of AHE in these systems, let alone the exploitation for optimal AHE.

Here, we first elaborate a general mechanism to increase $\mathcal{K}$ and thus AHC based on a model study with a single pair of Weyl nodes. Thereafter, we propose that FB in 3D systems can be a fertile ground for giant AHE where quasi double degenerate FBs can host multiple pairs of Weyl nodes with optimized $\mathcal{K}$. Finally, we examine the validity of this model in pyrochlore and spinel compounds through DFT calculations, and demonstrate its tunability through strain engineering. It is further applied to a more complicated magnetic WSM [21–23], $Co_3Sn_2S_2$, which shows a giant enhancement of AHE while lowering band dispersion.

WSM toy model We start from the cleanest scenario with one single pair of Weyl nodes with the Hamiltonian given by [39, 40]

$$\mathcal{H} = \tau_z \otimes [\mathbf{f}(\mathbf{k}) \cdot \sigma] + \tau_x \otimes [g(\mathbf{k})\sigma_0] + \tau_0 \otimes [(\beta/2)\sigma_x], \tag{1}$$

where $\mathbf{f}(\mathbf{k}) = \hat{x}t_x \sin(k_x a) + \hat{y}t_y \sin(k_y a) + \hat{z}t_z \sin(k_z a)$ and $g(\mathbf{k}) = t_x[1 - \cos(k_x a)] + t_y[1 - \cos(k_y a)] + t_z[1 - \cos(k_z a)]$; σ, a, and t are the Pauli matrices, lattice constant, and nearest neighbor (NN) hopping parameter, respectively; β defines the exchange splitting strength. Figure 1(a) displays a typical band structure with a pair of Weyl nodes located at $k = (\pm k_0, 0, 0)$ with $k_0 = \arccos[1 - \beta^2/(8t_x^2)]$ [41]. In particular, the momentum separation between the two Weyl nodes, $\mathcal{K} = 2k_0$, increases with the increase of β and/or the decrease of the hopping parameter t_x, as shown in Fig. 1(b).

The intrinsic AHC can be calculated by integrating Berry curvature of the occupied Block states, as prescribed by the Kubo formula [12]:

$$\Omega_n^x(\mathbf{k}) = -\sum_{n' \neq n} \frac{2\mathrm{Im}[\langle \phi_{n\mathbf{k}} \mid v_y \mid \phi_{n'\mathbf{k}} \rangle \langle \phi_{n'\mathbf{k}} \mid v_z \mid \phi_{n\mathbf{k}} \rangle]}{(\epsilon_{n'\mathbf{k}} - \epsilon_{n\mathbf{k}})^2}, \tag{2}$$

$$\sigma_{yz} = -\frac{e^2}{\hbar} \int_{BZ} \frac{d^3k}{(2\pi)^3} \sum_n f_{n\mathbf{k}} \Omega_n^x(\mathbf{k}). \tag{3}$$

To better understand how Berry curvature of Weyl pair contributes to the AHC, we show the Berry curvature distribution, Ω^x, at the $k_x - k_y$ plane in Fig. 1(c). The Berry curvature is mainly distributed in the vicinity of the Weyl nodes, and the linear scan shows that there are non-compensating Berry curvatures that contribute to the AHC [inset of Fig. 1(c)[41]]. We explicitly calculate AHC based on Eq. (3) as a function of β for different t_x values, which agrees perfectly with the AHC calculated based on $\mathcal{K}$ using $\sigma_{xy} = \frac{e^2\mathcal{K}}{4\pi^2}$, as shown in

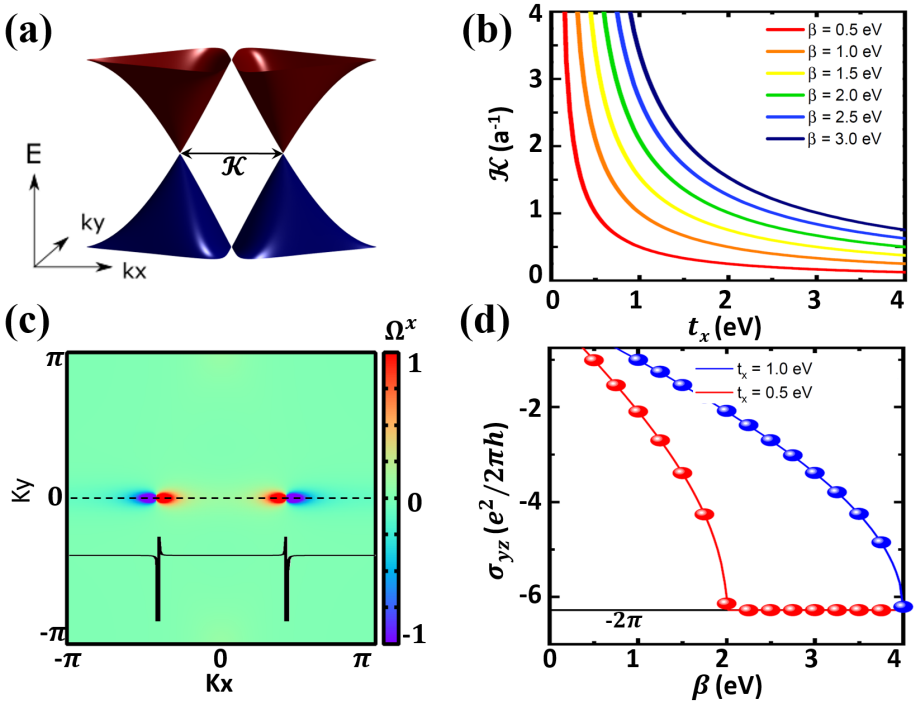

FIG. 1. **Band structure and anomalous Hall conductivity of generic WSMs.** (a) Typical band structure of a magnetic WSM derived from Eq. (1). We set an exchange field along the x direction and the following parameters: $\beta = 2$ eV, $t_x = t_y = t_z = 1$ eV and $a = 1$ Å . (b) Weyl node separation as a function of t_x for several β values. (c) Berry curvature (Ω^x) distribution at the $k_x - k_y$ plane with inset showing linear scan along the dashed line. (d) Calculated AHC based on Eq. (3) (symbols) and Weyl nodes separation ($\sigma_{xy} = \frac{e^2\mathcal{K}}{4\pi^2}$, solid curves) as a function of the exchange splitting strength β for different t_x values. The horizontal line highlights the maximum value -2π for which $\sigma_{yz} = e^2/h$.

Fig. 1(d). As anticipated, the AHC becomes larger with increasing $\mathcal{K}$ and could even reach the quantum limit of e^2/h when the system transition from WSM to Chern insulator state with $\mathcal{K} = 2\pi/a$ [41]. The results suggests that smaller t_x could enhance AHC, since smaller t_x implies larger $\mathcal{K}$.

Pyrochlore lattice tight-binding model Beyond the toy model, we extend our study to more realistic systems, where we can further verify the aforementioned mechanism and also explore promising material candidates. From band structure perspective, smaller t_x usually leads to narrower bands. The extreme scenario would be the FB case. Distinct from trivial FBs that are related to defect states [42, 43], here we will focus on nontrivial FBs system

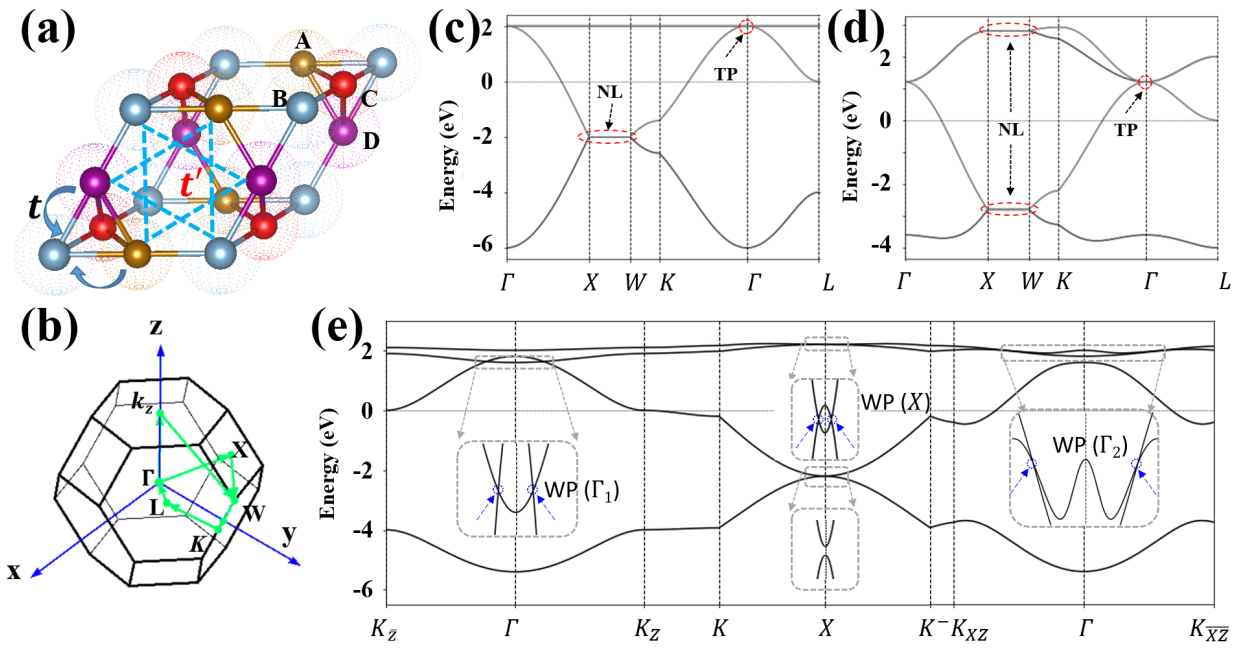

FIG. 2. **Band structure of pyrochlore lattice.** (a) Crystal structure of pyrochlore lattice with four atoms (A-D) in one unit cell. t and t' indicate the NN and NNN hoppings, respectively. (b) High symmetry k-path in the first Brillouin zone. (c) Band structure of ideal pyrochlore lattice without considering NNN interaction and SOC effect. (d) Band structure with NNN interaction t' = $0.2t$. The triple degenerate point (TP) and nodal lines (NL) are highlighted by red ellipses. (e) Band structure considering SOC (λ = -0.2t) and broken TRS ($\lambda_z = 5t$) with different Weyl points (WPs) highlighted.

due to destructive interference, e.g., in pyrochlore lattice [44, 45]. Pyrochlore lattice is a 3D network of corner-sharing tetrahedron [Fig. 2(a)], which contains four atoms in each unit cell. Considering one orbital on each atomic site and limit interactions to only the essential NN (t) and next NN (NNN, t') hoppings, the Hamiltonian can be written as:

$$\mathcal{H} = \sum_{i\sigma} \epsilon_i d^\dagger_{i\sigma} d_{i\sigma} - t \sum_{\langle i,j\rangle\sigma} d^\dagger_{i\sigma} d_{j\sigma} - t' \sum_{\langle\langle i,j\rangle\rangle\sigma} d^\dagger_{i\sigma} d_{j\sigma} + H.c., \tag{4}$$

where ϵ_i represents the on-site energy at site i.

For the ideal case with zero t' and uniform $\epsilon_i = 0$ and $t = 1$, we get two degenerate FBs, $E^{1,2} = 2t$ and two dispersive bands, $E^{3,4} = -2t(1\pm\sqrt{1+A_k})$, where $A_k = cos(2k_x)cos(2k_y)+ cos(2k_x)cos(2k_z) + cos(2k_y)cos(2k_z)$. One of the dispersive bands touches the FBs at the Γ point forming a triple degenerate point (TP) and two dispersive bands form nodal lines (NL)

along X-W and its symmetry invariant k-paths [Fig. 2(b) and (c)]. After considering the NNN hopping effect [41], the two FBs become dispersive and disperse upwards/downwards for positive/negative t'. As shown in Fig. 2(c), the evolution of the band structure shows the increase of bandwidth of FBs with increasing $|t'|$ [41]. The degeneracy of the two FBs is lifted, however, the TP and the NL feature remain robust [Fig. 2(d)]. [46]

To induce the magnetic WSM phase, we add a SOC (H_{SOC}) and a Zeeman type exchange splitting term (H_z) to our Hamiltonian: [37]

$$H_{SOC} = i\lambda \sum_{\langle\langle i,j\rangle\rangle\alpha\beta} (\overrightarrow{r_{ij}^{1}} \times \overrightarrow{r_{ij}^{2}}) \cdot \sigma_{\alpha\beta} s_{i\alpha}^{\dagger} s_{j\beta}, \tag{5}$$

$$H_z = \lambda_z \sum_{i\alpha} d_{i\alpha}^{\dagger} \sigma_z d_{j\alpha}, \tag{6}$$

where λ and λ_z describe the SOC and the exchange splitting strength, respectively. With only nonzero λ, the band structure shows that the TP at Γ point is splitted, and the NL degeneracy is also lifted except the X point, leading to various topological states [41]. After breaking the time reversal symmetry with nonzero λ_z, we achieve a magnetic WSM state, as shown in Fig. 2(e). The formation of Weyl points (WPs) can be more intuitively understood as the evolution of Dirac points (DPs) due to H_{SOC} and H_z induced perturbation [48], which lift DPs degeneracy and push flat band downward to cross the dispersive band, forming pairs of Weyl nodes, e.g., the WPs(Γ_1) along $k_z - \Gamma$ path arises from the DP at Γ point and similar for WP(X) and WP(Γ_2) that arise from DP at X and Γ, respectively [Fig. 2(e)] [41].

Anomalous Hall Effect With broken TRS in conjunction with SOC, various Weyl points are created near the FBs that serve as hotspots for Berry curvature. We calculate the intrinsic AHC (σ_{xy}) using Eq. (3). The upper branch of the band structure and AHC when $t' = 0, \lambda = 0.2t$, and $\lambda_z = 5t$ is shown in Fig. 3(a). The lower branch is symmetric to the upper branch, with the same AHC but opposite sign [41]. Clearly, there is a large peak right at the energy of the FBs, where multiple pairs of Weyl nodes are residing. To understand the correlation between flatness of FBs and the AHC, we study the evolution of AHC with different band dispersion by tuning t', as shown in Fig. 3(b). Evidently, with the increase of t', the bandwidth of the 'FBs' increases with a pronounced change in AHC. The single AHC peak splits into three different peaks with a noticeable degradation in the maximum AHC, as indicated by the arrows in Fig. 3(b).

By analyzing the evolution of band structure and AHC [Fig. 3(b)], we notice that the

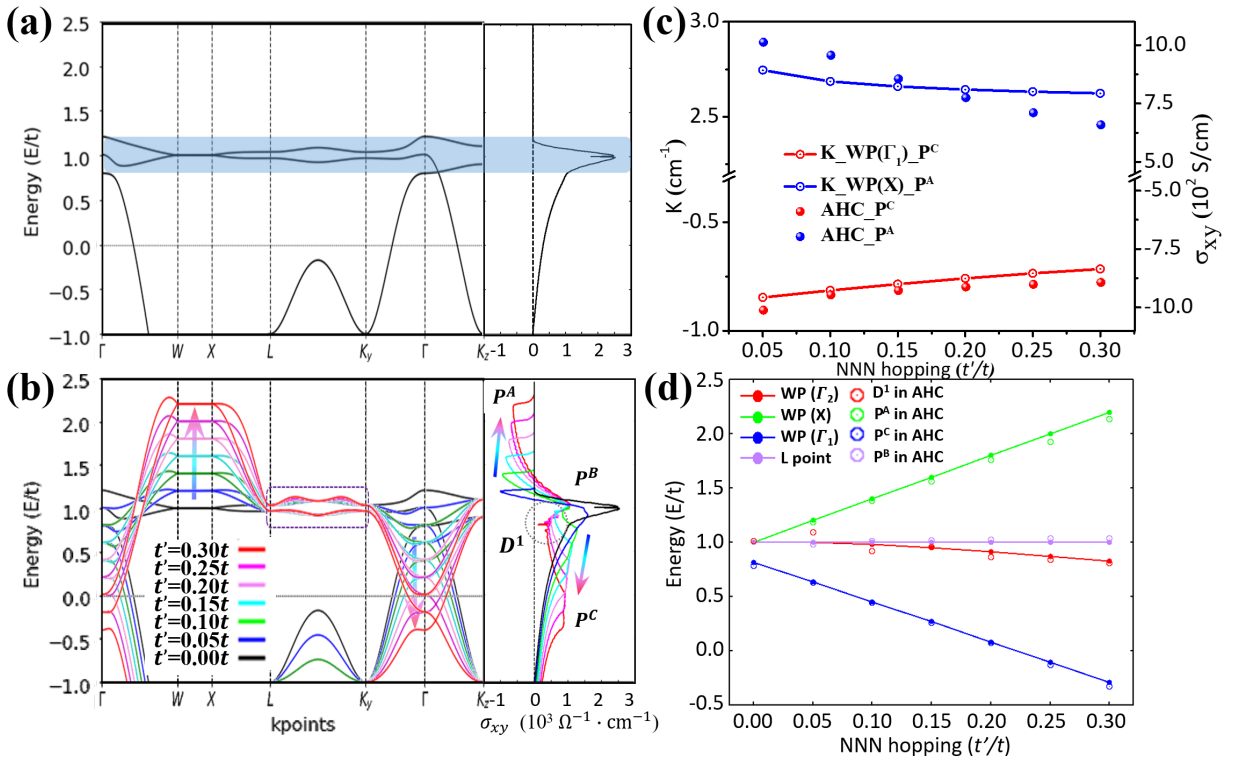

FIG. 3. **Evolution of AHC with the change of NNN hopping strength t'.** (a) Left and right panel shows band structure and AHC of the pyrochlore model with zero t'. (b) Same as (a) for evolution of the band structure and AHC with the change of NNN hopping strength t', respectively. AHC decreases with the increase of the band width due to the increase with the t', as indicated by the colored arrow.(c) Evolution of $\mathcal{K}$ for WP(Γ_1) and WP(X) and their corresponding AHC, $P^{C,A}$ with different t'. (d) Energy evolution of WP(Γ_1, X, Γ_2) and L point in comparison with evolution of peaks $P^{A,B,C}$ and D^1 with different t'.

energy of one of the splitted peaks, P^A, is shifting to higher energies with increasing t'. Its energy is always coincident with that of high-symmetry k-path $X-W$, which happens to be highly energetically degenerate with almost zero dispersion. Another peak, P^B, remains at the same energy level that corresponds to the energy of $L-K_y$ [dashed square in Fig. 3(b)], where the two bands remain nearly flat with very small energy difference [41]. Similarly, we find that the position of peak P^C is coincident with the position of the crossing point between bottom FB and upper Dirac band along $K_z-\Gamma$, shifting downward with the increasing t'. We note that there is also a small dip (D^1) between P^B and P^C, which also shifts to the lower energy with increasing t'.

To further validate the connection between the band dispersion and AHC, we calculate the position of Weyl nodes and Berry curvature related to $P^{A,B,C}$ and D^1. The crossing points between upper Dirac and lower FB are well isolated from the other bands, corresponding to an ideal magnetic WSM with one single pair of Weyl nodes [WP(Γ_1) in Fig. 2(e)] [41]. As expected, the Berry curvature is mainly distributed around Weyl nodes that contribute to P^C [41]. The broadening of the P^C is coincident with the energy gap at the Γ point, indicating the contribution of Berry curvature near the Γ point, which is reasonable because of the gap opening from Dirac state [41]. There exist another six pairs of Weyl nodes formed by the two 'FBs', among which three pairs are located symmetrically around the k_z axis along six directions [41]. The Berry curvature of the (001) plane crossing the Γ point shows large contributions from these Weyl points [41]. Possibly due to the type-II feature of these Weyl fermions, [WP(Γ_2) in Fig. 2(e)], it contributes negatively to the AHC (D^1) [19]. The other three pairs of Weyl nodes are near X and its symmetry-invariant k points [WP(X) in Fig. 2(e)] [41]. Similarly, significant Berry curvature contributes to P^A along $X-W$ path due to the very close energy between two FBs [41]. Interestingly, corresponding to the P^B, there are also large Berry curvature contributions from L and $L-K_y$ path even without existence of Weyl nodes [41].

To verify the linear relationship between momentum separation of Weyl pairs and AHC, $\sigma_{xy}=\frac{e^2\mathcal{K}}{4\pi^2}$, we extract $\mathcal{K}$ in comparison with its AHC with changing t', as shown in Fig. 3(c) [41]. The evolution of WP(Γ_1/X) show very good agreement with the change of AHC, $P^{C/A}$. The opposite sign in AHC for P^C and P^A is due to the opposite distribution of positive and negative Weyl nodes. Because of the type-II feature of WP(Γ_2) and the close distribution between D^1 and P^B, such relationship is not applicable to WP(Γ_2). We also plot the energy evolution of those Weyl nodes and AHC peaks, as shown in Fig. 3(d). The perfect agreement further verifies the contribution from each type of Weyl nodes to those AHC peaks. More importantly, when t' becomes smaller, energies of Weyl nodes for P^A, P^B and D^1 get closer to each other and that of L point, leading to the giant AHC observed for $t'=0$. This suggest the superimposing of multiple pairs of Weyl nodes due to the FBs with small band dispersion can indeed enhance the AHC.

With this tunable pyrochlore lattice model, we can also study the SOC (λ), exchange splitting (λ_z), and structural effect (lattice constant a) on the AHE. It is generally believed that large SOC is required to achieve large AHC [12, 15], which limits the searching of large

AHE materials in heavy metals. Surprisingly, our results show that the SOC has limited influence on the Weyl nodes separation and thus AHC [41]. Similar behavior is observed for different exchange splitting strength [41]. In addition, we also studied the effect of lattice constant, which shows smaller lattice will yield larger AHC [41]. This is consistent with $\sigma_{xy} = \frac{e^2\mathcal{K}}{4\pi^2}$, where $\mathcal{K}$ depends inversely with the real space lattice constant.

Pyrochlore and spinel compounds and beyond Further, using DFT calculations [41], we seek real materials within pyrochlore and spinel compounds [44, 45, 49, 50] that can be described by our TB model, which should yield giant AHC. The crystal structure of the $\alpha-$pyrochlore ($A_2B_2O_7$) and normal spinel compounds (AB_2O_4) are shown in Fig. 4(a) and (b), respectively. With proper selection of A and B cations with suitable valence electrons, we can realize the 3D FBs and the corresponding giant AHE. For the pyrochlore compounds, we choose $Nb_2Sn_2O_7$ as an example, which has been demonstrated to host the 3D FBs [36, 37]. However, the FBs are spin degenerated and located right below the Fermi level, which need hole doping to partial fill the FBs and trigger the spin splitting. Because of the large density of state and strong correlation effect, the band structure experiences a large spin splitting with even a small amount of hole doping, as shown in Fig. 4(c) for the system with one hole. The corresponding AHC is shown in Fig. 4(e), which indeed shows a large AHC peak near the FBs right at the Fermi level. However, due to the large lattice constant and the dispersive FBs, the peak value is not as large as the TB model. We also calculate $Nb_2Pb_2O_7$, which shows FBs with less dispersion and a corresponding enhancement of AHC [41, 47]. For the spinel compounds [20, 49], we study the MgV_2O_4 that hosts 3D FBs in its ferromagnetic state [38]. Due to orbital degeneracy, the band structure for MgV_2O_4 exhibits four FBs right above the Fermi level with the bandwidth much narrower than that in pyrochlore compounds [Fig. 4(d)]. Because of the higher degeneracy of FBs and their narrower bandwidth as well as a smaller lattice constant, we observe a much larger AHC, as shown in Fig. 4(f). We also calculate other spinel compounds that have similar band structure, which could all yield giant AHC [41].

Considering that Weyl pairs can be pictured as crossing points between two bands, originating from the perturbation of singular Dirac point [48], the decrease of band dispersion will always lead to increase of the Weyl pair separation $\mathcal{K}$ and thus the corresponding AHE until the two bands are fully separated [41]. To further confirm the generality of our proposal, we apply 4% tensile strain to decrease the hopping/band dispersion of two distinct

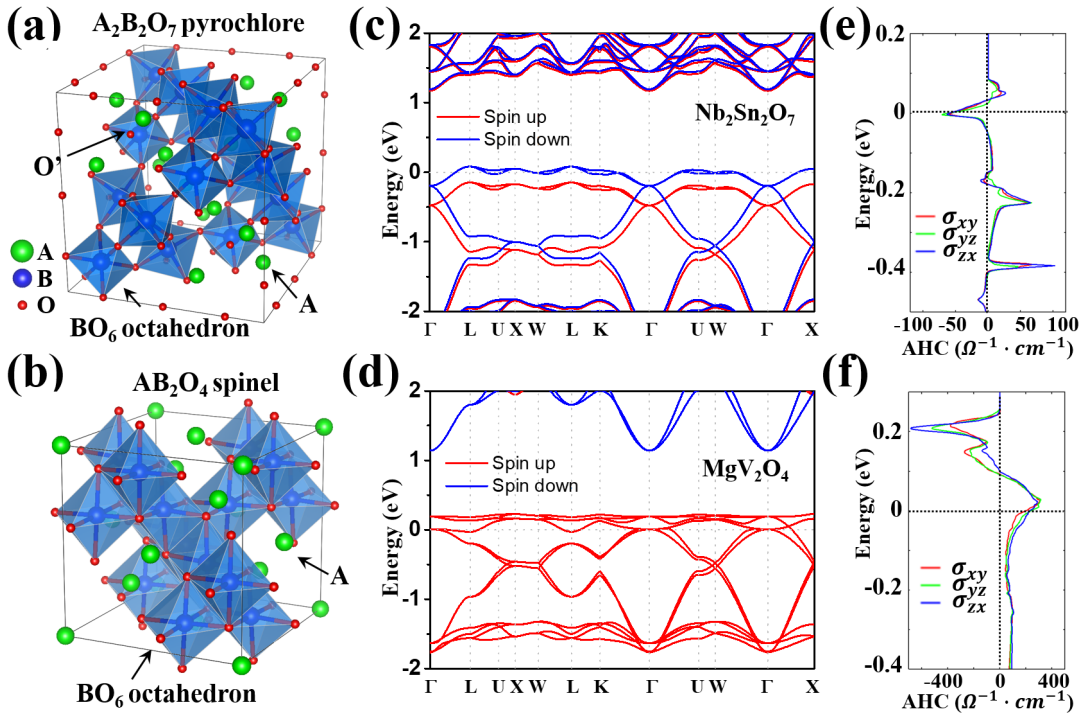

FIG. 4. **Giant AHE in pyrochlore and spinel compounds.** (a) Crystal structure of the pyrochlore compounds with the A cations forming the 3D kagome lattice. (b) Band structure of hole doped $Sn_2Nb_2O_7$. (c) DFT calculated AHC. (d) - (f) same as (a) - (c) for the spinel compounds MgV_2O_4, where cations B form the 3D kagome lattice.

magnetic WSM systems, i.e., $Nb_2Sn_2O_7$ and $Co_3Sn_2S_2$ [21–23]. Remarkably, we observe a giant increase (≈50%) of AHC for both $Nb_2Sn_2O_7$ that fits into FB lattice model and $Co_3Sn_2S_2$ with much complicated Weyl distribution [41].

Discussion and perspectives It is generally believed that AHE is proportional to the magnetization or strength of exchange splitting [1, 51]. Here, we demonstrate that the microscopic hopping could be engineered to enhance the AHE by increasing $\mathcal{K}$, i.e., reducing the electronic bandwidth of Weyl-related bands. Also, large SOC is no longer a necessity to achieve large AHE, it is possible to achieve giant AHE even in small SOC compounds, such as $Nb_2Sn_2O_7$. Considering the generality of the pyrochlore model and diversity of pyrochlore and spinel compounds, we expect to greatly expand the number of material candidates with giant AHE. We believe such phenomenon could also be generalized to other magnetic WSMs, which deserves further studies.

This project is supported by SMART, one of seven centers of nCORE, a Semiconductor

Research Corporation program, sponsored by National Institute of Standards and Technology (NIST). We acknowledge the MSI in the University of Minnesota for providing the computational resources.

* jiangw@umn.edu

† tlow@umn.edu

[1] N. Nagaosa, J. Sinova, S. Onoda, A. H. MacDonald, and N. P. Ong, Rev. Mod. Phys. **82**, 1539 (2010).

[2] J. Moritz, B. Rodmacq, S. Auffret, and B. Dieny, Journal of Physics D: Applied Physics **41**, 135001 (2008).

[3] Y. M. Lu, J. W. Cai, H. Y. Pan, and L. Sun, Applied Physics Letters **100**, 022404 (2012).

[4] K. Wang, Y. Zhang, and G. Xiao, Phys. Rev. Applied **13**, 064009 (2020).

[5] J.-P. Wang, S. S. Sapatnekar, C. H. Kim, P. Crowell, S. Koester, S. Datta, K. Roy, A. Raghunathan, X. S. Hu, M. Niemier, A. Naeemi, C.-L. Chien, C. Ross, and R. Kawakami, in *Proceedings of the 54th Annual Design Automation Conference 2017*, DAC '17 (Association for Computing Machinery, New York, NY, USA, 2017).

[6] D. C. Mahendra, R. Grassi, J.-Y. Chen, M. Jamali, D. Reifsnyder Hickey, D. Zhang, Z. Zhao, H. Li, P. Quarterman, Y. Lv, M. Li, A. Manchon, K. A. Mkhoyan, T. Low, and J.-P. Wang, Nature Materials **17**, 800 (2018).

[7] D. Zhang, M. Bapna, W. Jiang, D. P. de Sousa, Y.-C. Liao, Z. Zhao, Y. Lv, A. Naeemi, T. Low, S. A. Majetich, and J.-P. Wang, "Bipolar electric-field switching of perpendicular magnetic tunnel junctions through voltage-controlled exchange coupling," (2019), arXiv:arXiv:1912.10289.

[8] J. Puebla, J. Kim, K. Kondou, and Y. Otani, Communications Materials **1**, 24 (2020).

[9] J. Smit, Physica **21**, 877 (1955).

[10] L. Berger, Phys. Rev. B **2**, 4559 (1970).

[11] J. Ye, Y. B. Kim, A. J. Millis, B. I. Shraiman, P. Majumdar, and Z. Tešanović, Phys. Rev. Lett. **83**, 3737 (1999).

[12] Y. Yao, L. Kleinman, A. H. MacDonald, J. Sinova, T. Jungwirth, D.-S. Wang, E. Wang, and Q. Niu, Phys. Rev. Lett. **92**, 037204 (2004).

[13] S. Onoda, N. Sugimoto, and N. Nagaosa, Phys. Rev. Lett. **97**, 126602 (2006).

[14] R. Karplus and J. M. Luttinger, Phys. Rev. **95**, 1154 (1954).

[15] T. Jungwirth, Q. Niu, and A. H. MacDonald, Phys. Rev. Lett. **88**, 207208 (2002).

[16] D. Xiao, M.-C. Chang, and Q. Niu, Rev. Mod. Phys. **82**, 1959 (2010).

[17] A. A. Burkov and L. Balents, Phys. Rev. Lett. **107**, 127205 (2011).

[18] A. A. Burkov, Phys. Rev. Lett. **113**, 187202 (2014).

[19] A. A. Zyuzin and R. P. Tiwari, JETP Letters **103**, 717 (2016).

[20] W. Jiang, H. Huang, F. Liu, J.-P. Wang, and T. Low, Phys. Rev. B **101**, 121113 (2020).

[21] E. Liu, Y. Sun, N. Kumar, L. Muechler, A. Sun, L. Jiao, S.-Y. Yang, D. Liu, A. Liang, Q. Xu, J. Kroder, V. S., H. Borrmann, C. Shekhar, Z. Wang, C. Xi, W. Wang, W. Schnelle, S. Wirth, Y. Chen, S. T. B. Goennenwein, and C. Felser, Nature Physics **14**, 1125 (2018).

[22] Q. Wang, Y. Xu, R. Lou, Z. Liu, M. Li, Y. Huang, D. Shen, H. Weng, S. Wang, and H. Lei, Nature Communications **9**, 3681 (2018).

[23] C. Shekhar, N. Kumar, V. Grinenko, S. Singh, R. Sarkar, H. Luetkens, S.-C. Wu, Y. Zhang, A. C. Komarek, E. Kampert, Y. Skourski, J. Wosnitza, W. Schnelle, A. McCollam, U. Zeitler, J. Kübler, B. Yan, H.-H. Klauss, S. S. P. Parkin, and C. Felser, Proceedings of the National Academy of Sciences **115**, 9140 (2018).

[24] E. Derunova, Y. Sun, C. Felser, S. S. P. Parkin, B. Yan, and M. N. Ali, Science Advances **5** (2019), 10.1126/sciadv.aav8575.

[25] A. Mielke, Journal of Physics A: Mathematical and General **24**, L73 (1991).

[26] Z. Liu, F. Liu, and Y.-S. Wu, Chinese Physics B **23**, 077308 (2014).

[27] W. Jiang, M. Kang, H. Huang, H. Xu, T. Low, and F. Liu, Phys. Rev. B **99**, 125131 (2019).

[28] C. Wu, D. Bergman, L. Balents, and S. Das Sarma, Phys. Rev. Lett. **99**, 070401 (2007).

[29] E. Tang, J.-W. Mei, and X.-G. Wen, Phys. Rev. Lett. **106**, 236802 (2011).

[30] J. C. Budich and E. Ardonne, Phys. Rev. B **88**, 035139 (2013).

[31] W. Maimaiti, A. Andreanov, H. C. Park, O. Gendelman, and S. Flach, Phys. Rev. B **95**, 115135 (2017).

[32] W. Jiang, Z. Liu, J.-W. Mei, B. Cui, and F. Liu, Nanoscale **11**, 955 (2019).

[33] S. Nishino and M. Goda, Journal of the Physical Society of Japan **74**, 393 (2005).

[34] H.-M. Guo and M. Franz, Phys. Rev. Lett. **103**, 206805 (2009).

[35] C. Weeks and M. Franz, Phys. Rev. B **85**, 041104 (2012).

[36] I. Hase, T. Yanagisawa, Y. Aiura, and K. Kawashima, Phys. Rev. Lett. **120**, 196401 (2018).

[37] Y. Zhou, K.-H. Jin, H. Huang, Z. Wang, and F. Liu, Phys. Rev. B **99**, 201105 (2019).

[38] J. Azadani, W. Jiang, J.P Wang, and T. Low, Phys. Rev. B **102**, 155144(2020).

[39] M. M. Vazifeh and M. Franz, Phys. Rev. Lett. **111**, 027201 (2013).

[40] M. Istas, C. Groth, and X. Waintal, Phys. Rev. Research **1**, 033188 (2019).

[41] See Supplemental Material at [URL will be inserted by publisher] for methods, magnetic Weyl semimetal toy model, pyrochlore lattice tight-binding analysis, supplementary figures 1-9, and Supplementary tables 1 and 2..

[42] F. Corsetti and A. A. Mostofi, Phys. Rev. B **84**, 035209 (2011).

[43] L. Hu, H. Huang, Z. Wang, W. Jiang, X. Ni, Y. Zhou, V. Zielasek, M. G. Lagally, B. Huang, and F. Liu, Phys. Rev. Lett. **121**, 066401 (2018).

[44] B. C. Chakoumakos, Journal of Solid State Chemistry **53**, 120 (1984).

[45] J. S. Gardner, M. J. P. Gingras, and J. E. Greedan, Rev. Mod. Phys. **82**, 53 (2010).

[46] We note the Fermi level in the tight-binding model is artificial. The position of Fermi level will depends on number of electrons (occupancies) in real materials..

[47] We note that with reduced bandwidth of FBs, stronger correlation effect would induce larger exchange splitting, see more details in supporting information.

[48] J.-W. Rhim and B.-J. Yang, Phys. Rev. B **99**, 045107 (2019).

[49] R. J. Hill, J. R. Craig, and G. V. Gibbs, Physics and Chemistry of Minerals **4**, 317 (1979).

[50] K. E. Sickafus, J. M. Wills, and N. W. Grimes, JACS **82**, 3279 (1999).

[51] G. S. Thakur, P. Vir, S. N. Guin, C. Shekhar, R. Weihrich, Y. Sun, N. Kumar, and C. Felser, Chem. Mater. **32**, 1612 (2020).